

1 Detection of slow slip events using wavelet
2 analysis of GNSS recordings

3 Ariane Ducellier¹, Kenneth C. Creager², and David A. Schmidt²

4 ¹Corresponding author. University of Washington, Department of
5 Earth and Space Sciences, Box 351310, 4000 15th Avenue NE
6 Seattle, WA 98195-1310

7 ²University of Washington, Department of Earth and Space
8 Sciences

9 **Key points**

- 10 • We use a wavelet-based signal processing method to detect transients in
11 GNSS data, such as slow slip events.
- 12 • There is a good correlation between detections of slow slip using GNSS
13 data and using tremor data.
- 14 • The method could be applied in regions where no tremor is detected in
15 conjunction with slow slip events.

₁₆ **Abstract**

₁₇ In many places, tectonic tremor is observed in relation to slow slip and can
₁₈ be used as a proxy to study slow slip events of moderate magnitude where
₁₉ surface deformation is hidden in Global Navigation Satellite System (GNSS)
₂₀ noise. However, in subduction zones where no clear relationship between tremor
₂₁ and slow slip occurrence is observed, these methods cannot be applied, and we
₂₂ need other methods to be able to better detect and quantify slow slip. Wavelets
₂₃ methods such as the Discrete Wavelet Transform (DWT) and the Maximal
₂₄ Overlap Discrete Wavelet Transform (MODWT) are mathematical tools for
₂₅ analyzing time series simultaneously in the time and the frequency domain by
₂₆ observing how weighted differences of a time series vary from one period to the
₂₇ next. In this paper, we use wavelet methods to analyze GNSS time series and
₂₈ seismic recordings of slow slip events in Cascadia. We use detrended GNSS data,
₂₉ apply the MODWT transform and stack the wavelet details over several nearby
₃₀ GNSS stations. As an independent check on the timing of slow slip events,
₃₁ we also compute the cumulative number of tremor in the vicinity of the GNSS
₃₂ stations, detrend this signal, and apply the MODWT transform. In both time
₃₃ series, we can then see simultaneous waveforms whose timing corresponds to the
₃₄ timing of slow slip events. We assume that there is a slow slip event whenever
₃₅ there is a positive peak followed by a negative peak in the wavelet signal. We
₃₆ verify that there is a good correlation between slow slip events detected with only
₃₇ GNSS data, and slow slip events detected with only tremor data for northern
₃₈ Cascadia. The wavelet-based detection method detects well events of magnitude
₃₉ higher than 6 as determined by independent event catalogs (e.g. [Michel et al.,
₄₀ 2019]). **We then apply the wavelet method to data from New Zealand**
₄₁ **and detect slow slip events spatially and temporally close to those**
₄₂ **detected previously by Todd and Schwartz [2016].**

43 **1 Introduction**

44 Slow slip events are new **phenomena** discovered in the last two decades in
45 many subduction zones thanks to recordings of the displacement of Earth's sur-
46 face by dense Global Navigation Satellite System (GNSS) networks [Vergnolle
47 et al., 2010, Schmidt and Gao, 2010, Jiang et al., 2012, Wallace et al.,
48 2012]. As with ordinary earthquakes, slow slip events represent slip on a fault,
49 for instance the plate boundary between a tectonic plate subducting under an-
50 other tectonic plate. However, they take a much longer time (several days to
51 several years) to happen relative to ordinary earthquakes. They have a rela-
52 tively short recurrence time (months to years) compared to the recurrence time
53 of regular earthquakes (up to several hundreds of years), allowing scientists to
54 observe and study many complete event cycles, which is typically not possible
55 to explore with traditional earthquake catalogs [Beroza and Ide, 2011]. A slow
56 slip event on the plate boundary is inferred to happen when there is a reversal of
57 the direction of motion at GNSS stations, compared to the secular interseismic
58 motion. Slow slip events have been observed in many places [Beroza and
59 Ide, 2011, Audet and Kim, 2016], such as Cascadia [Bartlow, 2020],
60 Nankai [Nishimura et al., 2013], Alaska [Li et al., 2016], Costa Rica
61 [Jiang et al., 2012], Mexico [Radiguet et al., 2012], and New Zealand
62 [Wallace, 2020].

63

64 In many places, tectonic tremor is also observed in relation to slow slip, but
65 **the spatial correlation between tremor and slow slip may vary along**
66 **the strike of the plate boundary** [Hall et al., 2018]. Tremor is a long
67 (several seconds to many minutes), low amplitude seismic signal, with emer-
68 gent onsets, and an absence of clear impulsive phases. Tectonic tremor have
69 been explained as a swarm of small, low-frequency earthquakes (LFEs) [Shelly

et al., 2007], which are small magnitude earthquakes ($M \sim 1$) **whose** frequency content (1-10 Hz) is lower than for ordinary earthquakes (up to 20 Hz). In subduction zones such as Nankai and Cascadia, tectonic tremor observations are spatially and temporally correlated with slow slip observations [Rogers and Dragert, 2003, Obara et al., 2004]. Due to this correlation, these paired phenomena have been called Episodic Tremor and Slip (ETS). However, this is not always the case. For instance, in northern New Zealand, tremor is more challenging to detect, and seems to be located downdip of the slow slip on the plate boundary [Todd and Schwartz, 2016]. In Alaska, the tremor zone only partially overlaps the long-term slow slip zone and there does not appear to be any temporal correlation between tremor and slow slip occurrence [Wech, 2016].

81

In Cascadia, there are robust signals in both GNSS and tremor [Hawthorne and Rubin, 2013]. This is also the case in Nankai [Hiramatsu et al., 2008], where tiltmeters are used instead of GNSS. It is thus possible to use tremor as a proxy to observe slow slip events that are not directly observed in the GNSS data. For instance, Aguiar et al. [2009] studied 23 ETS events in Cascadia with more than 50 hours of tectonic tremor. For all these events, they computed both the GPS-estimated moment release and the cumulative number of hours of tectonic tremor recorded. They observed a linear relationship between moment release and number of hours of tremor for **slow slip** events of moment magnitude 6.3 to 6.8. Based on this linear relationship, it is possible to infer the existence of smaller slow slip events of magnitude 5-6 occurring simultaneously with smaller tremor bursts of duration 1 to 50 hours occurring in between the big ETS events, and for which there is no detectable signal in the GPS data.

95

Frank [2016] divided GPS time series observations from Cascadia and Guer-

97 rero, Mexico, into two groups: the first group contains days with abundant
98 tremor and LFEs, the second group contains days when the number of tremor
99 or LFEs is lower than a threshold. He then stacked separately the two groups
100 of daily observations and observed a cumulative displacement in the direction
101 corresponding to the loading period when few tremor or LFEs are observed
102 and the surface deformation corresponds to the secular plate motion. He also
103 observed a cumulative displacement in the opposite direction corresponding to
104 the release period when tremor and LFEs are observed. He was thus able to
105 observe a reverse displacement corresponding to smaller slow slip events not
106 directly observable in the GPS data for individual events.

107

108 However, these methods cannot be applied to detect slow slip events in places
109 where tremor and slow slip occurrence are not well spatially and temporally cor-
110 related, tremor is not abundant, or the seismic network is not robust enough.
111 We thus need other methods to be able to better detect and quantify slow slip.

112

113 Wavelet methods such as the Discrete Wavelet Transform (DWT) are math-
114 ematical tools for analyzing time series simultaneously in the time and the fre-
115 quency domain by observing how weighted differences of a time series vary from
116 one period to the next. Wavelet methods have been widely used for geophysical
117 applications (e.g. Kumar and Foufoula-Georgiou [1997]). However, few studies
118 have used wavelet methods to analyze recordings of slow slip, and their scope
119 was limited to the detection of the bigger (magnitude 6-7) short-term (a few
120 weeks) events [Szeliga et al., 2008, Ohtani et al., 2010, Wei et al., 2012, Alba
121 et al., 2019].

122

123 Szeliga et al. [2008] determined the timing and the amplitude of 34 slow

124 slip events throughout the Cascadia subduction zone between 1997 and 2005
125 using wavelets. They modeled the GPS time series by the sum of a linear trend,
126 annual and biannual sinusoids representing seasonal effects, Heaviside step func-
127 tions corresponding to earthquakes and hardware upgrades, and a residual sig-
128 nal. They then applied a Gaussian wavelet transform to the residual time series
129 to get the exact timing of slow slip at each GPS station. The idea is that the
130 wavelet transform allows us to analyze the signal both in the time and the fre-
131 quency domains. A sharp change in the signal will be localized and seen at all
132 **time scales** of the wavelet decomposition, contrary to what happens with the
133 periodic sinusoids of the Fourier transform.

134

135 Instead of using wavelets in the time domain, Ohtani et al. [2010] used 2D
136 wavelet functions in the spatial domain to detect slow slip events. They de-
137 signed the Network Stain Filter (NSF) to detect transient deformation signals
138 from large-scale geodetic arrays. They modeled the position of the GPS station
139 by the sum of the secular velocity, a spatially coherent field, site-specific noise,
140 reference frame errors, and observation errors. The spatial displacement field is
141 modeled by the sum of basis wavelets with time-varying weights. Their method
142 has been successfully used to detect a transient event in the Boso peninsula,
143 Japan, and a slow slip event in the Alaska subduction zone [Wei et al., 2012].

144

145 Finally, Alba et al. [2019] used hourly water level records from four tide
146 gauges in the Juan de Fuca Straight and the Puget Sound to determine relative
147 vertical displacements associated with **slow slip** events between 1996 and 2011.
148 Their main idea is that the tidal level measured at a given gauge is the sum of
149 a noise component at multiple timescales (tides, ocean and atmospheric noise)
150 and an uplift signal due to the **slow slip** events. The noise component is as-

151 sumed to be coherent between all tidal gauges, while the tectonic uplift signal is
152 different provided that the gauges are far enough from each other. By stacking
153 the tidal records after removing tides, the uplift signals cancel each other while
154 the noise signal is amplified. By stacking the **components at different time**
155 **scales** of the DWT decomposition, instead of stacking the raw tidal record,
156 each of the components of the noise at different time scales is retrieved and
157 can then be removed from the raw records to obtain the uplift signal. **Due**
158 **to the relative location of the tidal gauges at Port Angeles and Port**
159 **Townsend compared to the slow slip region on the plate boundary, a**
160 **slow slip event should result in uplift in Port Angeles (western part)**
161 **and in subsidence in Port Townsend (eastern part).** Indeed, the au-
162 **thors were able to clearly see a difference in the sign of the uplift at**
163 **these two tidal gauges.**

164

165 In our study, we use a similar approach to previous studies with a different
166 reasoning. We only stack signals at nearby GPS stations, assuming that the
167 **east-west** displacement due to the **slow slip** events will then be the same at
168 each of the GPS stations considered. We suppose that some of the noise com-
169 ponent is different at each GPS station and will be eliminated by the stacking.
170 Finally, we assume that the noise and the longitudinal displacement due to the
171 **slow slip** events and the secular plate motion have different time scales, so
172 that the wavelet decomposition will act as a bandpass filter to retrieve the dis-
173 placement signal and highlight the **slow slip** events. We use wavelet methods
174 to analyze GPS and tremor recordings of slow slip events in Cascadia. Our
175 objective is to verify that there is a good correlation between slow slip events
176 detected with only GNSS data, and slow slip events detected with only tremor
177 data. We thus want to demonstrate that the wavelet-based detection method

178 can be applied to detect slow slip events that may currently be obscured using
179 standard methods. **Finally, we apply the method to GPS data in New
180 Zealand and successfully detect several slow slip events without need-**
181 **ing to rely on the tremor data.**

182

183 2 Data

184 We **first** focused our study on northwest Washington State. For the GNSS
185 data, we used the GPS time series provided by the Pacific Northwest Geode-
186 tic Array, Central Washington University. These are network solutions **in**
187 **ITRF2014 with phase ambiguities resolved with wide-lane phase-**
188 **biases and orbits and satellite clocks provided by the Jet Propulsion**
189 **Laboratory/NASA.** North, East, and Vertical directions are available. How-
190 ever, as the direction of the secular plate motion is close to the East direction,
191 we only used the East direction of the GPS time series for the data analysis, as
192 it has the best signal-to-noise ratio. The wavelet method works best with data
193 with zero mean, and no sharp discontinuities; so we use the cleaned dataset,
194 that is GPS times series with linear trends, steps due to earthquakes or hard-
195 ware upgrades, and annual and semi-annual sinusoids signals simultaneously
196 estimated and removed following Szeliga et al. [2004]. For the tremor data, we
197 used the tremor catalog from the Pacific Northwest Seismic Network (PNSN)
198 [Wech, 2010].

199

200 **For the application to slow slip events in New Zealand, we used**
201 **the GPS time series provided by the Geological hazard information**
202 **for New Zealand (GeoNet). The coordinates have been extracted by**
203 **GeoNet during the GLOBK run from the combined daily solution**

204 files, and converted to (east, north, up) displacement in millimeters
205 with respect to an a priori position and epoch in the ITRF2008 re-
206 alization. The time series provided by GeoNet have no adjustments
207 made to them, so they may, for example, contain offsets due to earth-
208 quakes, offsets due to equipment changes at individual sites, and sea-
209 sonal (annual and semi-annual) signals due to various causes. Here
210 again, the direction of the secular plate motion is close to the West
211 direction, so we only used the East direction of the GPS time series
212 for the data analysis. We detrended the data before applying the
213 wavelet transform by carrying a linear regression of the whole time
214 series and removing the straight line obtained from the regression.

215 3 Method

216 3.1 The Maximal Overlap Discrete Wavelet Transform

217 The Discrete Wavelet Transform (DWT) is an orthonormal transform that
218 transforms a time series X_t ($t = 0, \dots, N - 1$) into a vector of wavelet coeffi-
219 cients W_i ($i = 0, \dots, N - 1$). If we denote J the level of the wavelet decom-
220 position, and the number of observations is equal to $N = n * 2^J$, where n is
221 some integer greater than or equal to 1, the vector of wavelet coefficients
222 can be decomposed into J wavelet vectors W_j of lengths $\frac{N}{2}, \frac{N}{4}, \dots, \frac{N}{2^J}$, and
223 one scaling vector V_J of length $\frac{N}{2^J}$. Each wavelet vector W_j is associated with
224 changes on time scale $\tau_j = dt2^{j-1}$, where dt is the time step of the time se-
225 ries, and corresponds to the filtering of the original time series with a filter
226 with nominal frequency interval $[\frac{1}{dt2^{j+1}}; \frac{1}{dt2^j}]$. The scaling vector V_J is assici-
227 ated with averages in time scale $\lambda_J = dt2^J$, and corresponds to the filtering of
228 the original time series with a filter with nominal frequency interval $[0; \frac{1}{dt2^{j+1}}]$.

229 Wavelet vectors can be further decomposed into details and smooths, which are
 230 more easily interpretable. We define for $j = 1, \dots, J$ the j th wavelet detail
 231 D_j , which is a vector of length N , and is associated to time scale $\tau_j = dt2^{j-1}$.
 232 Similarly, we can define for $j = 1, \dots, J$ the j th wavelet smooth S_j , which is a
 233 vector of length N , and is associated to scales $\tau_{j+1} = dt2^{j+1}$ and higher. The
 234 basic idea is to reapply to W_j the wavelet filter that was used to construct W_j
 235 from the initial time series X . Together, the details and the smooths define the
 236 multiresolution analysis (MRA) of X :

$$237 \quad X = \sum_{j=1}^J D_j + S_J \quad (1)$$

238 The DWT presents several disadvantages. First, the length of the time se-
 239 ries must be a multiple of 2^J where J is the level of the DWT decompositon.
 240 Second, the time step of the wavelet vector W_j is $dt2^j$, which may not corre-
 241 spond to the time when some interesting phenomenon is visible on the original
 242 time series. Third, when we circularly shift the time series, the corresponding
 243 wavelet coefficients, details and smooths are not a circularly shifted version of
 244 the wavelet coefficients, details and smooths of the original time series. Thus,
 245 the values of the wavelet coefficients, details and smooths are strongly dependent
 246 on the time when we start experimentally gathering the data. Finally, when we
 247 filter the time series to obtain the details D_j and smooths S_j , we introduce a
 248 phase shift, which makes it difficult to line up meaningfully the features of the
 249 MRA with the original time series.

250

251 To overcome the disadvantages described above, we use instead the Maxi-
 252 mal Overlap Discrete Wavelet Transform (MODWT). The MODWT transforms
 253 the time series X_t ($t = 0, \dots, N - 1$) into J wavelet vectors \tilde{W}_j ($j = 1, \dots, J$) of
 254 length N and a scaling vector \tilde{V}_J of length N . As is the case for the DWT,

255 each wavelet vector \widetilde{W}_j is associated with changes on scale $\tau_j = dt2^{j-1}$, and
 256 corresponds to the filtering of the original time series with a filter with nominal
 257 frequency interval $[\frac{1}{dt2^{j+1}}; \frac{1}{dt2^j}]$. The scaling vector \widetilde{V}_J is associated with aver-
 258 ages in scale $\lambda_J = dt2^J$, and corresponds to the filtering of the original time
 259 series with a filter with nominal frequency interval $[0; \frac{1}{dt2^{J+1}}]$. As is the case for
 260 the DWT, we can write the MRA:

$$261 \quad X = \sum_{j=1}^J \widetilde{D}_j + \widetilde{S}_J \quad (2)$$

262 The MODWT of a time series can be defined for any length N . The time
 263 step of the wavelet vectors \widetilde{W}_j and the scaling vector \widetilde{V}_J is equal to the time
 264 step of the original time series. When we circularly shift the time series, the
 265 corresponding wavelet vectors, scaling vector, details and smooths are shifted
 266 by the same amount. The details and smooths are associated with a zero phase
 267 filter, making it easy to line up meaningfully the features of the MRA with the
 268 original time series. The wavelet methods for time series analysis are explained
 269 in a more detailed way in [Percival and Walden, 2000]).
 270

271 3.2 Application to synthetic data

272 To illustrate the wavelet transform method, we first apply the MODWT to syn-
 273 thetic data. As slow slip events occur in Cascadia on a regular basis, every
 274 twelve to eighteen months, we create a synthetic signal of period $T = 500$ days.
 275 To reproduce the ground displacement observed on the longitudinal component
 276 of GPS stations in Cascadia, we divide each period into two parts: In the first
 277 part of duration $T - N$, the displacement is linearly increasing and corresponds
 278 to the inter seismic plate motion in the eastern direction; in the second part
 279 of duration N , the displacement is linearly decreasing and corresponds to a

280 slow slip event on a reverse fault at depth triggering a ground displacement in
281 the western direction. To see the effect of the duration of the slow slip event,
282 we use different values for $N = 5, 10, 20, 40$ days. The amplitude of the set is
283 normalized to 1. Figure 1 shows the synthetics, the details D_j of the wavelet
284 decomposition for levels 1 to 10, and the smooth S_{10} for the four durations of a
285 slow slip event.

286

287 The ramp-like signal is transformed through the wavelet filtering into a wave-
288 form with first a positive peak and then a negative peak. The shape of the wave-
289 form is the same for every level of the wavelet decomposition, but the width of
290 the waveform increases with the scale level. For the 8th level of the wavelet de-
291 composition, the width of the waveform is nearly as large as the time between
292 two events. At larger scales, the waveforms start to merge two contiguous events
293 together, and make the wavelet decomposition less interpretable. For an event
294 of duration 5 days, the wavelet details at levels higher than 3 have a larger
295 amplitude than the wavelet details at lower scales. For an event of duration 10
296 days, the wavelet details at levels higher than 4 have a larger amplitude than
297 the wavelet details at lower scales. For an event of duration 20 days, the wavelet
298 details at levels higher than 5 have a larger amplitude than the wavelet details
299 at lower scales. For an event of duration 40 days, the wavelet details at levels
300 higher than 6 have a larger amplitude than the wavelet details at lower scales.
301 Thus, the scale levels at which an event is being seen in the wavelet details give
302 us an indication about the duration (and the magnitude) of the slow slip event.
303 The big slow slip events of magnitude 6-7 typically trigger a signal that lasts
304 about one week at an individual GPS station, and the whole event lasts several
305 weeks. We expect them to start being visible at the level 5 of the wavelet de-
306 composition, but to not be noticeable at lower time scales.

308 3.3 MODWT of GPS and tremor data

309 The DWT and MODWT methods must be used on a continuous time series,
 310 without gaps in the recordings. To deal with the gaps in the GNSS recordings,
 311 we simply replace the missing values by interpolation. The value for the first
 312 day for which data are missing is equal to the mean of the five days before
 313 the gap. The value for the last day for which data are missing is equal to the
 314 mean of the five days after the gap. The remaining missing values are com-
 315 puted by doing a linear interpolation of the first and the last values and adding
 316 a Gaussian noise component with mean zero and standard deviation equal to
 317 the standard deviation of the whole time series. We verify how the wavelet
 318 details may be affected by looking at a GPS time series without missing values
 319 and compared the wavelet details with and without removing some data points.
 320 Station PGC5 recorded continuous 1390 days between 2009 and 2013 without
 321 any missing values. We first computed the wavelet details without missing val-
 322 ues. Then, we removed ten neighboring values, replaced them using the method
 323 described above (linear interpolation plus Gaussian noise), and computed the
 324 wavelet details with the replaced values. **Figure S1 in the Supplementary**
 325 **Material** shows a comparison of the two wavelet details for two different lo-
 326 cations of the missing values. We can see that there are visible differences in
 327 the time series itself, and in the details at the smallest levels of the wavelet
 328 decomposition. However, the differences between the wavelet details with and
 329 without missing values get smaller and smaller with increasing levels of details,
 330 and are barely visible for the levels that are most relevant (levels 6 and above).
 331 We thus conclude that we can easily replace the missing values in the GNSS
 332 time series without introducing false detections of slow slip events.

333

334 We then applied the wavelet filtering to real GPS data. Figure 2 shows the
335 longitudinal displacement for GPS station PGC5, located in southern Vancouver
336 Island, the details of the wavelet decomposition for levels 1 to 8, and the
337 smooth. In the data, we can see a sharp drop in displacement whenever there is
338 a documented slow slip event. For levels 5 to 8, which correspond to time scales
339 16, 32, 64 and 128 days, we can see in the details a positive peak followed by
340 a negative peak whenever there is a drop in displacement in the data. We thus
341 verify that the wavelet method can detect steps in the time series associated
342 with slow slip events.

343

344 To increase the signal-to-noise ratio and better detect slow slip events, we
345 stack the signal from several neighboring GPS stations. We choose to focus on
346 GPS stations located close enough to the tremor zone to get a sufficiently high
347 amplitude of the slow slip signal. We choose 16 points along the 40 km depth
348 contour of the plate boundary (model from Preston et al. [2003]) with spacing
349 equal 0.1 degree in latitude (red triangles on Figure 3). Then we took all the
350 GPS stations located in a 50 km radius for a given point, compute the wavelet
351 details for the longitudinal displacement of each station, and stack each detail
352 over the GPS stations. We thus have a stacked detail for each level 1 to 10 of
353 the wavelet decomposition.

354

355 To assess the success of the wavelet decomposition for detecting slow slip
356 events in GPS time series, we validate the approach by comparing to an inde-
357 pendent proxy for **slow slip** events. We took all the tremor epicenters located
358 within a 50 km radius centered on one of the 16 locations marked by red trian-
359 gles on Figure 3. Then we computed the cumulative number of tremor within

360 this circle. Finally, we removed a linear trend from the cumulative tremor count,
361 and applied the wavelet transform. Figure 4 shows an example of the wavelet
362 decomposition for the third northernmost location on Figure 3 (which is closest
363 to GPS station PGC5). Contrary to what happens for the GPS data, we see
364 a sharp increase in the time series whenever there is a tremor episode, which
365 translates into a negative peak followed by a positive peak in the wavelet details.

366 4 Application to data from Cascadia

367 We stacked the 8th level detail of the wavelet decomposition of the displacement
368 over all the GPS stations located in a 50 km radius of a given point, for the 16
369 locations indicated in Figure 3. The result is shown in the top panel of Figure 5,
370 where each line represents one of the locations along strike. To better highlight
371 the peaks in the wavelet details, we highlighted in red the time intervals where
372 the amplitude of the stacked detail is higher than a threshold, and in blue the
373 time intervals where the amplitude of the stacked detail is lower than minus the
374 threshold. To compare the GPS signal with the tremor signal, we plotted the
375 8th level detail of the wavelet decomposition of the tremor count on the bottom
376 panel of Figure 5. We multiplied by -1 the cumulative tremor count for the
377 wavelet decomposition in order to be able to match positive peaks with positive
378 peaks and negative peaks with negative peaks. In the tremor catalog from the
379 PNSN, there are 17 tremor events with more than 150 hours of tremor recorded.
380 The events are summarized in Table 1. The time of the event is the start date
381 plus half the duration of the event.

382
383 Although the latitudinal extension of the events is not always the same for
384 the GPS data and for the tremor data, we identify the same 13 events in both 8th
385 wavelet decompositions for the 8th level: January 2007, May 2008, May 2009,

386 August 2010, August 2011, September 2012, September 2013, August-November
387 2014, January 2016, March 2017, June 2018, March-November 2019, and Oc-
388 tober 2020-January 2021. Although there are two events in the tremor catalog
389 in August 2014 and November 2014, these two events are not distinguishable in
390 the 8th level details and look more like a single event slowly propagating from
391 South to North. The same phenomenon is observed in 2019 when two tremor
392 events in March and November 2019 are merged into a single event propagating
393 slowly from South to North. In 2020-2021, the wavelet decomposition of the
394 tremor shows one event in the south in October-November 2020 and one event
395 in the North in January 2021, but in the wavelet decomposition of the GPS
396 data, these three events look like a single event propagating slowly from South
397 to North.

398

399 A similar comparison is shown for the wavelet decomposition of the GPS
400 data and the wavelet decomposition of the tremor count data for the 7th level
401 and the 6th level respectively (Figures 6 and 7). The events are harder to see in
402 the 7th level than in the 8th level, both for the GPS data and the tremor count
403 data. The wavelet decomposition is more noisy for the GPS data between 2010
404 and 2012, but it does not seem that there are more slow slip events visible in
405 the 7th level.

406

407 For the 6th level detail, we see an additional event in the South in Fall 2009
408 that is present both in the GPS and the tremor data. It may correspond to the
409 northern extent of a big ETS event occurring in Fall 2009 south of the study
410 area (event 19 in the Michel et al. [2019] catalog). There are three small sig-
411 nals in the GPS data in Winter 2012, Fall 2017, and Winter 2020 that are not
412 present in the tremor data, and may be false detections. To summarize, we

413 assume that **robust** detections are events present in both GPS and tremor time
 414 series, and false detections are events present in the GPS but not in the tremor
 415 time series. Then, all the 13 events present on the 8th level detail of the wavelet
 416 decomposition are **robust** detections and 14 of the 17 events present on the 6th
 417 level detail of the wavelet decomposition are **robust** detections.

418

419 To better evaluate the number of **robust** and false detections, we convert
 420 the wavelet details into **trinary** time series. If the absolute value of the wavelet
 421 detail is higher than a threshold, we replace the value by 1 (for positive values)
 422 or -1 (for negative values), otherwise we replace the value by 0. We do this
 423 on both the wavelet details of the GPS data and of the tremor data. Then we
 424 decide that if both the GPS and the tremor time series take the value 1 (or
 425 both take the value -1), we have a **robust** detection (true positive, TP). If the
 426 GPS and the tremor time series have opposite signs, or if the absolute value of
 427 the GPS time series is 1 but the value of the tremor time series is 0, we have a
 428 false detection (false positive, FP). If both time series take the value 0, we do
 429 not have detection (true negative, TN). If the GPS time series take the value
 430 0, but the absolute value of the tremor time series is 1, we miss a detection
 431 (false negative, FN). We then define the sensitivity (true positive rate) and the
 432 specificity (equal to 1 minus the false positive rate) as:

$$\begin{aligned}
 \text{sensitivity} &= \frac{TP}{TP + FN} \\
 \text{specificity} &= \frac{TN}{TN + FP}
 \end{aligned} \tag{3}$$

433 We can then evaluate the quality of the detections obtained with our method
 434 by plotting a receiver operating characteristic curve (ROC curve). The ROC
 435 curve is widely used for binary classification problems in statistics and machine
 436 learning. We calculate an ROC value by varying the values of the threshold

437 (here the two thresholds used to convert the GPS and the tremor time series
438 into **trinary** time series), computing the corresponding values of the true pos-
439 itive rate and the false positive rate (equal to 1 minus the specificity), and
440 plotting the true positive rate as a function of the false positive rate. If the
441 classification was made randomly, all the points would fall on the first diagonal.
442 If the classifier was perfect, the corresponding point would fall on the top left
443 corner of the graph with true positive rate equal to 1 and false positive rate equal
444 to 0. The bigger the area under the curve, the better the classification method is.

445

446 As the slow slip events are better seen on levels 6, 7 and 8 of the wavelet
447 decomposition, we first add the wavelet details corresponding to levels 6 to 8,
448 and transform the resulting time series into a **trinary** time series. We apply
449 this transform to both the GPS and the tremor time series with varying thresh-
450 olds. We then plot the ROC curve on Figure 8, each dot representing a different
451 threshold. The corresponding sums of the wavelet details for the GPS data and
452 the tremor data are shown on Figure 9. We can see that there is a trade-off
453 between sensitivity and specificity as we vary the threshold. If we decrease the
454 false positive rate, we also decrease the number of true events detected. If we
455 increase the number of true events detected, we also increase the false positive
456 rate. **If we increase the threshold for the tremor, the curve goes far-**
457 **ther away from the first diagonal, that is we get better classification**
458 **results. If we increase the threshold for the GPS, the false positive**
459 **rate and the the number of events detected decrease.** In Figure 9, we
460 have chosen thresholds for the GPS time series and the tremor time series such
461 that the specificity is higher than 0.75 (**that is the false positive rate is**
462 **lower than 0.25**), and the sensitivity is the highest possible, that is we have
463 chosen the thresholds corresponding to the dot that is farthest from the diagno-

464 nal, which is random.

465

466 In addition to the magnitude 6 events discussed above, Michel et al. [2019]
467 have also identified several magnitude 5 events using a variational Bayesian In-
468 dependent Component Analysis (vbICA) decomposition of the signal. As we
469 expect smaller magnitude events to be more visible at smaller time scales of the
470 wavelet decomposition (level 5), we verify for all these events whether a signal
471 can be seen at the same time as the time given in their catalog. Most of these
472 magnitude 5 events are also sub-events of bigger magnitude 6 events. Table 2
473 summarizes for each event its timing, its number and its magnitude as indi-
474 cated in the catalog from Michel et al. [2019], and whether it is part of a bigger
475 magnitude 6 event. Figure 10 shows the 5th level detail wavelet decomposition
476 of the GPS data. Red lines show the timing of the big **slow slip** events from
477 Table 1, and blue lines show the timing of the small slow slip events from Table 2.

478

479 All 14 events that are sub-events of a bigger event are visible at level 5.
480 However, this may be because the bigger events are clearly seen at levels 6 to 8,
481 and also at smaller time scales. The one small event that is not part of a bigger
482 event (Winter 2009) is visible at level 5 of the wavelet decomposition. However,
483 some other events that are not in the catalog of Michel et al. [2019]’s catalog
484 are also visible in late 2007, early 2010, early 2012, and late 2016. Therefore,
485 it is difficult to differentiate between a **robust** detection and a false detection,
486 and to conclude whether the method can indeed detect events of magnitude 5.

487

488 In Figure 9, we see four smaller events that are not in the catalog of Michel
489 et al. [2019]: at about 2007.5, there is a negative peak followed by a positive
490 peak (that is an event in the opposite direction of what would be expected from

491 slow slip), at about 2010.2, 2012.2 and 2020.2, there are positive peaks followed
492 by negative peaks for all the sixteen locations studied in this paper. Looking
493 back at the original GPS data, there is a small increase in the displacement
494 in the eastern direction that lasts about one or two months at about 2007.5.
495 However, the direction of the displacement does not correspond to a slow slip
496 event, and another cause should be found to explain this signal. There is a de-
497 crease in displacement that lasts several months at about 2010.2. This transient
498 may correspond to a long duration slow slip event. There is a small decrease
499 in displacement at about 2012.2. Its amplitude is small but the duration and
500 direction correspond to a slow slip event, so this transient could be a very small
501 slow slip event. Finally, there is also a small decrease in displacement at about
502 2020.2 that is difficult to interpret.

503

504 **Due to the short distances between the GPS stations and the loca-**
505 **tions of the red triangles on the map from Figure 3, the same station**
506 **could be used multiple times for the stacking at different locations.**
507 **When considering two different locations, the stacking is thus made**
508 **over an overlapping number of stations. Table 3 summarizes the**
509 **number of stations and the number of overlapping stations for each**
510 **location on Figure 3. We hypothesize that the small displacement in**
511 **the eastern direction seen at about 2007.5 could be due to a misbe-**
512 **having station common to several locations. However, several GPS**
513 **stations indeed show an increase in the displacement in the eastern**
514 **direction at about 2007.5. There are many missing data around that**
515 **time, so it is difficult to conclude.**

516

517 **Another possibility is that common mode signals could stack con-**

518 structively across GNSS stations and produce peaks in the wavelet de-
519 tails that are actually due to non-tectonic signals. We computed com-
520 mon mode signals for different latitude bins (each bin has width equal
521 to half-a-degree of latitude) following the same method as Nuyen and
522 Schmidt [2021]. We first stacked all the time series for the stations
523 in each latitude bin that are located more than 100 km east of the
524 40 km depth contour of the plate boundary. We assume that these
525 stations are not sensitive to the deformation on the plate interface.
526 We then apply a yearly moving average to each common mode signal
527 in order to remove any leftover noise. The common mode signal was
528 then removed from the GNSS time series depending on each sites
529 latitude. Figure S2 in the Supplementary Information shows the cor-
530 responding sum of the stacks of the 6th, 7th and 8th wavelet details
531 obtained from the resulting time series. The common modes seem
532 to have little impact on the results and do not explain the additional
533 four small events that we noted in Figure 9.

534 5 Application to data from New Zealand

535 We now apply our wavelet-based method to detect slow slip events
536 in New Zealand. The tectonics of the North Island of New Zealand
537 are dominated by the westward subduction of the Pacific Plate un-
538 der the Australian Plate at the Hikurangi Trench. Two types of
539 slow slip events have been observed at the Hikurangi margin. Shal-
540 low (10-15 km depth), shorter (1-3 weeks), and usually smaller (Mw
541 6.3-6.8) slow slip events have been observed every 18-24 months in
542 the northern part of the margin. Deeper (35-60 km depth), longer
543 (12-18 months), and larger (Mw 7.0) slow slip events have been ob-

544 served every 5 years in the southern part of the margin [Wallace
545 and Beavan, 2010, Todd and Schwartz, 2016]. It used to be thought
546 that there were no tremor associated with slow slip events in north-
547 ern Hikurangi. Delahaye et al. [2009] observed an increase in the
548 rate of microseismicity downdip of the 2004 Gisborne slow slip event.
549 More recently, however, [Kim et al., 2011] detected a low level of
550 tremor activity that increased during the 2010 Gisborne slow slip
551 event. As was the case for the microearthquakes, the source of the
552 tremor was located downdip of the slow slip patch determined from
553 GNSS data. [Ide, 2012] detected tremor downdip of the location of
554 two deep slow slip events observed by Wallace and Eberhart-Phillips
555 [2013] in 2006 and 2008. However, contrary to ETS events in Casca-
556 dia and Nankai, the tremor activity did not seem to increase during
557 the slow slip events. Todd and Schwartz [2016] detected tremor
558 associated with most of the shallow slow slip events between 2010
559 and 2015, and located downdip of the geodetically inferred slip area.
560 They also detected deeper tremor between 20 and 50 km depth with
561 unclear origin. They hypothesized that these tremor may be related
562 to currently undetected deep long-term slow slip events.

563

564 As we have done for Cascadia, we take all GPS stations located
565 in a 50 km radius of a given point, for the 18 locations indicated in
566 Figure 11, and we stack the 6th level details, the 7th level details or
567 the 8th level details over all the GPS stations. We then sum together
568 the 6th, 7th and 8th levels stacked wavelet details (Figure 12, top
569 panel). We highlight positive and negative peaks with red and blue
570 colors as was done in Figure 9. As we cannot use the tremor data

571 to decide what is the appropriate threshold above which we consider
572 that there is a slow slip event, we assume that slow slip events in New
573 Zealand will result in a surface displacement of the same amplitude as
574 the displacement observed in Cascadia. Therefore, the amplitudes of
575 the peaks in the wavelet details should also be the same and we take
576 identical thresholds for both regions. As a slow slip event in north-
577 ern New Zealand results in a displacement in the east direction at the
578 Earths surface, the slow slip events are indicated by a negative peak
579 followed by a positive peak in the stacked wavelet details. We com-
580 pare the results to the timings and locations of the slow slip events
581 detected by Todd and Schwartz [2016]. As they only used data from
582 five GPS stations (PUKE? ANAU, GISB, MAHI and CKID), we in-
583 dicate by a vertical grey bar on the bottom panel of Figure 12 each
584 time a slow slip event was detected for this stations. The grey bars
585 are centered on the latitudes of the GPS stations. If a slow slip event
586 was detected by more than one station, all the corresponding grey
587 bars are linked together to show the spatial extent of the slow slip.
588 Todd and Schwartz [2016] indicated by a question mark (on their
589 Figure 2 and their Table 1) additional possible events, and those are
590 indicated by a dotted grey bar on Figure 12.

591

592 We observed that there is a good correlation between the events
593 detected with the wavelet method and the events previously detected
594 by Todd and Schwartz [2016]. It is unclear if the event near station
595 ANAU in early 2010 (event 1 from Todd and Schwartz [2016]) is
596 visible in the wavelet details, but we clearly see an event propagat-
597 ing from south to north in January-February and March-April 2010,

598 (events 2 and 3 from Todd and Schwartz [2016]). The June-July
599 2010 event (event 4 in Todd and Schwartz [2016]) and the August
600 2010 event (event 5 in Todd and Schwartz [2016]) are not clearly
601 visible in the wavelet details. There is an event in April-May 2011
602 in the northern part of the region studied (events 6 and 7 in Todd
603 and Schwartz [2016]). We then see an event propagating south to
604 north in August-September and September-October 2011 (events 8
605 and 9 in Todd and Schwartz [2016]), followed by another event in
606 December 2011 (event 10 in Todd and Schwartz [2016]). Although
607 [Todd and Schwartz, 2016] only detected this event for GPS station
608 GISB, it seems that this event may have also extended farther to the
609 north and the south. We do not detect event 11 from Todd and
610 Schwartz [2016] in March 2012 with our wavelet method. We then
611 see a slow slip event in the northern part of the region studied in
612 August 2012 (event 12 in Todd and Schwartz [2016]), followed by
613 another event in December 2012-January 2013 (event 13 in Todd
614 and Schwartz [2016]). There is a slow slip event in the southern part
615 of the region studied in February-March 2013 (event 14 in Todd and
616 Schwartz [2016]). We can an event propagating from south to north
617 in June-July and July-August 2013 (events 15 and 16 in Todd and
618 Schwartz [2016]). The events in September-October 2013, Decem-
619 ber 2013 and May-June 2014 (events 17, 18 and 19 in Todd and
620 Schwartz [2016]) are not clearly seen in the wavelet details, but there
621 could be a small negative peak followed by a small positive peak at
622 these times. We can then see a big slow slip event in September 2014
623 (events 20 and 21 in Todd and Schwartz [2016]) and a slow slip event
624 in the southern part of the region studied in December 2014-January

625 2015 (events 22 and 23 in Todd and Schwartz [2016]). The events
626 in January–February and February 2015 (events 24 and 25 in Todd
627 and Schwartz [2016]) are not clearly visible in the wavelet details, but
628 there could be a small negative peak followed by a small positive peak
629 at these times. Finally, we can see an event in June–July 2015 in the
630 northern part of the region studied (event 26 in Todd and Schwartz
631 [2016]). Additionally, there could be two other events that are not in
632 [Todd and Schwartz, 2016] in Fall 2010 (southern part of the region
633 studied) and in Fall 2015.

634

635 Our wavelet-based method thus works well to detect transients in
636 GPS data that could be slow slip events, even in the absence of tremor
637 data. The choice of the appropriate threshold to decide that there is
638 a transient and the levels of the wavelet details that we look at for
639 the detection may still not be easily made. In particular, as there
640 is more time between two slow slip events in New Zealand than in
641 Cascadia, the biggest slow slip events (early 2010, late 2011, 2013 and
642 late 2014) can also be seen on the 9th level detail for New Zealand,
643 whereas they could not be seen for Cascadia.

644

645 6 Conclusion

646 In this paper, we develop and test a new approach for detecting transient events
647 in GPS time series, such as slow slip events. We used wavelet methods to an-
648 alyze GNSS time series and tremor recordings of slow slip events in Cascadia,
649 and GNSS time series in New Zealand. We used detrended GNSS data,
650 applied the MODWT transform, and stacked the wavelet details over several

651 nearby GNSS stations. As an independent check on the timing of slow slip
652 events, we also computed the cumulative number of tremor in the vicinity of
653 the GNSS stations, detrended this signal, and applied the MODWT transform.
654 In both time series, we could then see simultaneous waveforms whose timing
655 corresponds to the timing of slow slip events. We assumed that there is a slow
656 slip event whenever the wavelet signal gets above a threshold. We verified that
657 there is a good correlation between slow slip events detected with only GNSS
658 data, and slow slip events detected with only tremor data. The wavelet-based
659 detection method detects all events of magnitude higher than 6 as determined
660 by independent event catalogs (e.g. [Michel et al., 2019]). We detected signals
661 in the GPS data that could be magnitude 5 events, but it is not easy to dif-
662 ferentiate between **robust** detections and false detections. **We then applied**
663 **the method to GNSS data in New Zealand and detected slow slip**
664 **events consistent with the events previously detected by Todd and**
665 **Schwartz [2016].**

666 Data and Resources

667 The GPS recordings used for this analysis can be downloaded from the PANGA
668 website [GPS/GNSS Network and Geodesy Laboratory: Central Washington
669 University, other/seismic network, 1996] <http://www.panga.cwu.edu/>. The
670 Python scripts used to analyze the data and make the figures can be found
671 on the first author's Github account <https://github.com/ArianeDucellier/>
672 **slowlip**. Figures 3 and 11 were created using GMT [Wessel and Smith, 1991].

673 **Acknowledgements**

674 The authors would like to anonymous reviewers and the Associate Editor Jeanne
675 Hardback, whose comments greatly helped improve the manuscript. This work
676 was funded by the grant from the National Science Foundation EAR-1358512.
677 A.D. would like to thank Professor Donald Percival for introducing her to
678 wavelet methods during his excellent class on Wavelets: Data Analysis, Al-
679 gorithms and Theory taught at University of Washington.

680 **Declaration of Competing Interests**

681 The authors declare no competing interests.

682 **References**

- 683 A.C. Aguiar, T.I. Melbourne, and C.W. Scrivner. Moment release rate of Cas-
684 cadia tremor constrained by GPS. *J. Geophys. Res.*, 114:B00A05, 2009.
- 685 S. Alba, R. J. Weldon, D. Livelybrooks, and D. A. Schmidt. Cascadia ETS
686 events seen in tidal records (1980–2011). *Bull. Seismol. Soc. Am.*, 109(2):
687 812–821, 2019.
- 688 P. Audet and Y.H. Kim. Teleseismic constraints on the geological environment
689 of deep episodic slow earthquakes in subduction zone forearcs: A review.
690 *Tectonophysics*, 670:1–15, 2016.
- 691 N. M. Bartlow. A longterm view of episodic tremor and slip in Cascadia. *Geo-*
692 *physical Research Letters*, 43(3):e2019GL085303, 2020.
- 693 G.C. Beroza and S. Ide. Slow earthquakes and nonvolcanic tremor. *Annu. Rev.*
694 *Earth Planet. Sci.*, 39:271–296, 2011.

- 695 E.J. Delahaye, J. Townend, M.E. Reyners, and G. Rogers. Microseismicity but
696 no tremor accompanying slow slip in the Hikurangi subduction zone, New
697 Zealand. *Earth and Planetary Science Letters*, 277:21–28, 2009.
- 698 W.B. Frank. Slow slip hidden in the noise: The intermittence of tectonic release.
699 *Geophys. Res. Lett.*, 43:10125–10133, 2016.
- 700 GPS/GNSS Network and Geodesy Laboratory: Central Washington University,
701 other/seismic network. Pacific Northwest Geodetic Array (PANGA), 1996.
702 URL <http://www.panga.cwu.edu/>.
- 703 K. Hall, H. Houston, and D. Schmidt. Spatial comparisons of tremor and slow
704 slip as a constraint on fault strength in the northern Cascadia subduction
705 zone. *Geochemistry, Geophysics, Geosystems*, 19(8):2706–2718, 2018.
- 706 J. C. Hawthorne and A. M. Rubin. Shorttime scale correlation between slow
707 slip and tremor in Cascadia. *Journal of Geophysical Research: Solid Earth*,
708 118:1316–1329, 2013.
- 709 Y. Hiramatsu, T. Watanabe, and K. Obara. Deep lowfrequency tremors as a
710 proxy for slip monitoring at plate interface. *Geophysical Research Letters*, 35:
711 L13304, 2008.
- 712 S. Ide. Variety and spatial heterogeneity of tectonic tremor worldwide. *Journal*
713 *of Geophysical Research*, 117:B03302, 2012.
- 714 Y. Jiang, S. Wdowinski, T. H. Dixon, M. Hackl, M. Protti, and V. Gonzalez.
715 Slow slip events in Costa Rica detected by continuous GPS observations,
716 2002-2011. *Geochemistry, Geophysics, Geosystems*, 13:Q04006, 2012.
- 717 M.J. Kim, S.Y. Schwartz, and S. Bannister. Nonvolcanic tremor associated with
718 the March 2010 Gisborne slow slip event at the Hikurangi subduction margin,
719 New Zealand. *Geophysical Research Letters*, 38:L14301, 2011.

- 720 P. Kumar and E. Foufoula-Georgiou. Wavelet analysis for geophysical applica-
721 tions. *Rev. Geophys.*, 35(4):385–412, 1997.
- 722 S. Li, J. Freymueller, and R. McCaffrey. Slow slip events and timedependent
723 variations in locking beneath Lower Cook Inlet of the AlaskaAleutian sub-
724 duction zone. *Journal of Geophysical Research: Solid Earth*, 121:1060–1079,
725 2016.
- 726 S. Michel, A. Gualandi, and J.-P. Avouac. Interseismic coupling and slow slip
727 events on the Cascadia megathrust. *Pure Appl. Geophys.*, 176:3867–3891,
728 2019.
- 729 T. Nishimura, T. Matsuzawa, and K. Obara. Detection of shortterm slow slip
730 events along the Nankai Trough, southwest Japan, using GNSS data. *Journal*
731 *of Geophysical Research: Solid Earth*, 118:3112–3125, 2013.
- 732 C. P. Nuyen and D. A. Schmidt. Filling the gap in Cascadia: The emergence of
733 lowamplitude longterm slow slip. *Geochemistry, Geophysics, Geosystems*, 22
734 (3):e2020GC009477, 2021.
- 735 K. Obara, H. Hirose, F. Yamamizu, and K. Kasahara. Episodic slow slip events
736 accompanied by non-volcanic tremors in southwest Japan subduction zone.
737 *Geophysical Research Letters*, 31:L23602, 2004.
- 738 R. Ohtani, J.J. McGuire, and P. Segall. Network strain filter: A new tool for
739 monitoring and detecting transient deformation signals in GPS arrays. *J.*
740 *Geophys. Res.*, 115:B12418, 2010.
- 741 D.B. Percival and A.T. Walden. *Wavelet Methods for Time Series Analysis*.
742 Cambridge Series in Statistical and Probabilistic Mathematics. Cambridge
743 University Press, New York, NY, USA, 2000.

- 744 L.A. Preston, K.C. Creager, R.S. Crosson, T.M. Brocher, and A.M. Trehu.
745 Intraslab earthquakes: Dehydration of the Cascadia slab. *Science*, 302:1197–
746 1200, 2003.
- 747 M. Radiguet, F. Cotton, M. Vergnolle, M. Campillo, A. Walpersdorf, N. Cotte,
748 and V. Kostoglodov. Slow slip events and strain accumulation in the Guerrero
749 gap, Mexico. *Journal of Geophysical Research: Solid Earth*, 117:B04305, 2012.
- 750 G. Rogers and H. Dragert. Tremor and slip on the Cascadia subduction zone:
751 The chatter of silent slip. *Science*, 300(5627):1942–1943, 2003.
- 752 D. A. Schmidt and H. Gao. Source parameters and timedeependent slip distribu-
753 tions of slow slip events on the Cascadia subduction zone from 1998 to 2008.
754 *Journal of Geophysical Research: Solid Earth*, 115:B00A18, 2010.
- 755 D.R. Shelly, G.C. Beroza, and S. Ide. Non-volcanic tremor and low-frequency
756 earthquake swarms. *Nature*, 446:305–307, 2007.
- 757 W. Szeliga, T.I. Melbourne, M.M. Miller, and V.M. Santillan. Southern Casca-
758 dia episodic slow earthquakes. *Geophys. Res. Lett.*, 31:L16602, 2004.
- 759 W. Szeliga, T. Melbourne, M. Santillan, and M. Miller. GPS constraints on 34
760 slow slip events within the Cascadia subduction zone, 1997-2005. *J. Geophys.*
761 *Res.*, 113:B04404, 2008.
- 762 E.K. Todd and S.Y. Schwartz. Tectonic tremor along the northern Hikurangi
763 Margin, New Zealand, between 2010 and 2015. *J. Geophys. Res. Solid Earth*,
764 121:8706–8719, 2016.
- 765 M. Vergnolle, A. Walpersdorf, V. Kostoglodov, P. Tregoning, J. A. Santiago,
766 N. Cotte, and S. I. Franco. Slow slip events in Mexico revised from the
767 processing of 11 year GPS observations. *Journal of Geophysical Research:*
768 *Solid Earth*, 115:B08403, 2010.

- 769 L. M. Wallace. Slow slip events in New Zealand. *Annual Review of Earth and*
770 *Planetary Sciences*, 48:175–203, 2020.
- 771 L. M. Wallace, J. Beavan, S. Bannister, and C. Williams. Simultaneous longterm
772 and shortterm slow slip events at the Hikurangi subduction margin, New
773 Zealand: Implications for processes that control slow slip event occurrence,
774 duration, and migration. *Journal of Geophysical Research: Solid Earth*, 117:
775 B11402, 2012.
- 776 L.M. Wallace and J. Beavan. Diverse slow slip behavior at the Hikurangi sub-
777 duction margin, New Zealand. *Journal of Geophysical Research*, 115:B12402,
778 2010.
- 779 L.M. Wallace and D. Eberhart-Phillips. Newly observed, deep slow slip events
780 at the central Hikurangi margin, New Zealand: Implications for downdip vari-
781 ability of slow slip and tremor, and relationship to seismic structure. *Geo-*
782 *physical Research Letters*, 40:5393–5398, 2013.
- 783 A.G. Wech. Interactive tremor monitoring. *Seismol. Res. Lett.*, 81(4):664–669,
784 2010.
- 785 A.G. Wech. Extending Alaska’s plate boundary; tectonic tremor generated by
786 Yakutat subduction. *Geology*, 44(7):587–590, 2016.
- 787 M. Wei, J.J. McGuire, and E. Richardson. A slow slip event in the south central
788 Alaska Subduction Zone. *Geophys. Res. Lett.*, 39:L15309, 2012.
- 789 P. Wessel and W. H. F. Smith. Free software helps map and display data. *EOS*
790 *Trans. AGU*, 72:441, 1991.
- 791 C. A. Williams, D. Eberhart-Phillips, S. Bannister, D. H. Barker, S. Henrys,
792 M. Reyners, and R. Sutherland. Revised interface geometry for the Hikurangi

⁷⁹³ subduction zone, New Zealand. *Seismological Research Letters*, 84(6):1066–
⁷⁹⁴ 1073, 2013.

⁷⁹⁵ **Addresses**

⁷⁹⁶ Ariane Ducellier. University of Washington, Department of Earth and Space
⁷⁹⁷ Sciences, Box 351310, 4000 15th Avenue NE Seattle, WA 98195-1310.

⁷⁹⁸

⁷⁹⁹ Kenneth C. Creager. University of Washington, Department of Earth and
⁸⁰⁰ Space Sciences, Box 351310, 4000 15th Avenue NE Seattle, WA 98195-1310.

⁸⁰¹

⁸⁰² David A. Schmidt. University of Washington, Department of Earth and
⁸⁰³ Space Sciences, Box 351310, 4000 15th Avenue NE Seattle, WA 98195-1310.

Tables

Table 1: Episodic Tremor and Slip events with $M \geq 6$ identified by MODWT in both the GPS and the tremor data. The duration and the number of tremor are from the tremor catalog of the PNSN. The event number and the magnitude are from the slow slip catalog of Michel et al. [2019].

Time	Duration (days)	Number of tremor (hours)	Event number	Magnitude
2007.06	28	398	3	6.68
2008.36	25	402	10	6.56
2009.35	24	248	16	6.49
2010.63	29	518	24	6.54
2011.60	37	479	30	6.47
2012.72	37	620	34	6.54
2013.71	27	423	41	6.58
2014.65	15	190	48	6.03
2014.89	38	385	51	6.40
2016.11	43	421	54	6.79
2017.23	19	279	59	6.61
2018.49	22	381		
2019.23	34	195		
2019.88	16	205		
2020.79	26	193		
2020.86	12	162		
2021.09	14	230		

Table 2: Magnitude 5 events from Michel et al. [2019].

Time	Event number	Magnitude	Sub-event of bigger event
2007.06	1	5.64	Yes
2007.08	2	5.91	Yes
2008.38	11	5.50	Yes
2009.16	14	5.50	No
2009.36	17	5.32	Yes
2010.63	25	5.76	Yes
2011.66	31	5.61	Yes
2011.66	32	5.32	Yes
2012.69	35	5.56	Yes
2013.74	42	5.71	Yes
2014.69	49	5.31	Yes
2014.93	52	5.39	Yes
2016.03	57	5.80	Yes
2017.13	60	5.43	Yes
2017.22	61	5.37	Yes

Table 3: Number of GPS stations used for the stacking for each location on Figure 3 and number of common stations with the location immediately to the north and the location immediately to the south.

Index	Latitude	Number of stations	Common stations (north)	Common stations (south)
0	47.2	15	14	
1	47.3	18	17	14
2	47.4	24	20	17
3	47.5	21	20	20
4	47.6	22	14	20
5	47.7	17	12	14
6	47.8	13	8	12
7	47.9	10	9	8
8	48.0	10	7	9
9	48.1	8	7	7
10	48.2	10	8	7
11	48.3	9	9	8
12	48.4	9	5	9
13	48.5	7	5	5
14	48.6	6	5	5
15	48.7	5		5

Figure captions

- Figure 1. Demonstration of a wavelet decomposition for a synthetic dataset.
A synthetic time series is created (top row) with steps of period 500 days, and transient durations of 2 days (left), 5 days, 10 days, and 20 days (right). The resulting details and smooths are shown in increasing level. The amplitude of the synthetic time series is normalized to 1, and the details and smooths show the relative amplitude.
- Figure 2. Top: Longitudinal displacement recorded at GPS station PGC5. The resulting details and smooth of the wavelet decomposition are shown in increasing level.
- Figure 3. GPS stations used in this study (black triangles). The black line represents the 40 km depth contour of the plate boundary model by Preston et al. [2003]. The red triangles are the locations where we stack

- 818 the GPS data. The small grey dots are all the tremor locations from the
 819 PNSN catalog.
- 820 • Figure 4. Details and smooth of the wavelet decomposition of the de-
 821 trended cumulative tremor count around the third northernmost red tri-
 822 angles on Figure 3 (latitude 48.5).
- 823 • Figure 5. Top: Stacked 8th level details of the wavelet decomposition of
 824 the displacement over all the GPS stations located in a 50 km radius of a
 825 given point, for the 16 red triangles indicated in Figure 3. Bottom: 8th
 826 level detail multiplied by -1 of the cumulative tremor count in a 50 km
 827 radius of a given point for the same 16 locations. The black lines represent
 828 the timings of the ETS events from Table 1. We mark by a red rectangle
 829 every time where the amplitude is higher than a threshold of 0.4 (for the
 830 GPS) or 0.003 (for the tremor). We mark by a blue rectangle every time
 831 where the amplitude is lower than minus the threshold.
- 832 • Figure 6. Same as Figure 5 but for the 7th level detail. The thresholds
 833 are 0.5 (for the GPS) and 0.01 (for the tremor).
- 834 • Figure 7. Same as Figure 5 but for the 6th level detail. The thresholds
 835 are 0.3 (for the GPS) and 0.009 (for the tremor).
- 836 • Figure 8. ROC curve for the sum of the 6th, 7th, and 8th level details of
 837 the wavelet decomposition. Each dot represents the true positive rate of
 838 event detections and the false positive rate of event detections for a given
 839 pair of thresholds (for the GPS and for the tremor). The **black** cross
 840 marks the true positive rate and the false positive rate obtained with the
 841 thresholds used to make Figure 9. **The values of the threshold are**
 842 **color-coded. Reds correspond to the lowest value of the thresh-**
 843 **old for the tremor (0.001), while oranges, greens, blues, purples**

844 correspond to increasing values of the threshold for the tremor
845 (up to 0.01). The brightest colors correspond to the highest
846 values of the threshold for the GPS (1.5), while the darker and
847 darker colors correspond to decreasing values of the threshold
848 for the GPS (0.1).

849 • Figure 9. Same as Figure 5 but for the sum of the 6th, 7th and 8th level
850 details. The thresholds are 0.8 (for the GPS) and 0.01 (for the tremor).

851 • Figure 10. Top: Stacked 5th level details of the wavelet decomposition
852 of the displacement over all the GPS stations located in a 50 km radius
853 of a given point, for the 16 red triangles indicated in Figure 3. The red
854 lines represent the timings of the ETS events from Table 1. The blue
855 lines represent the timings of the magnitude 5 events from the catalog of
856 Michel et al. [2019].

857 • **Figure 11.** GPS stations used for the slow slip detection in New
858 Zealand (black triangles). The red triangles are the locations
859 where we stack the GPS data. They are located close to the 20
860 km depth contour of the plate boundary from Williams et al.
861 [2013].

862 • **Figure 12.** Top: Sum of the stacked 6th, 7th and 8th level
863 details of the wavelet decomposition of the displacement over
864 all the GPS stations located in a 50 km radius of a given point,
865 for the 18 red triangles indicated in Figure 11. We mark by a
866 red rectangle every time where the amplitude is higher than a
867 threshold equal to 0.4. We mark by a blue rectangle every time
868 where the amplitude is lower than minus the threshold. Bottom:
869 Sum of the stacked 6th, 7th and 8th level details of the wavelet

⁸⁷⁰ decomposition. We mark with a grey bar the slow slip events
⁸⁷¹ detected by Todd and Schwartz [2016].

872 **Figures**

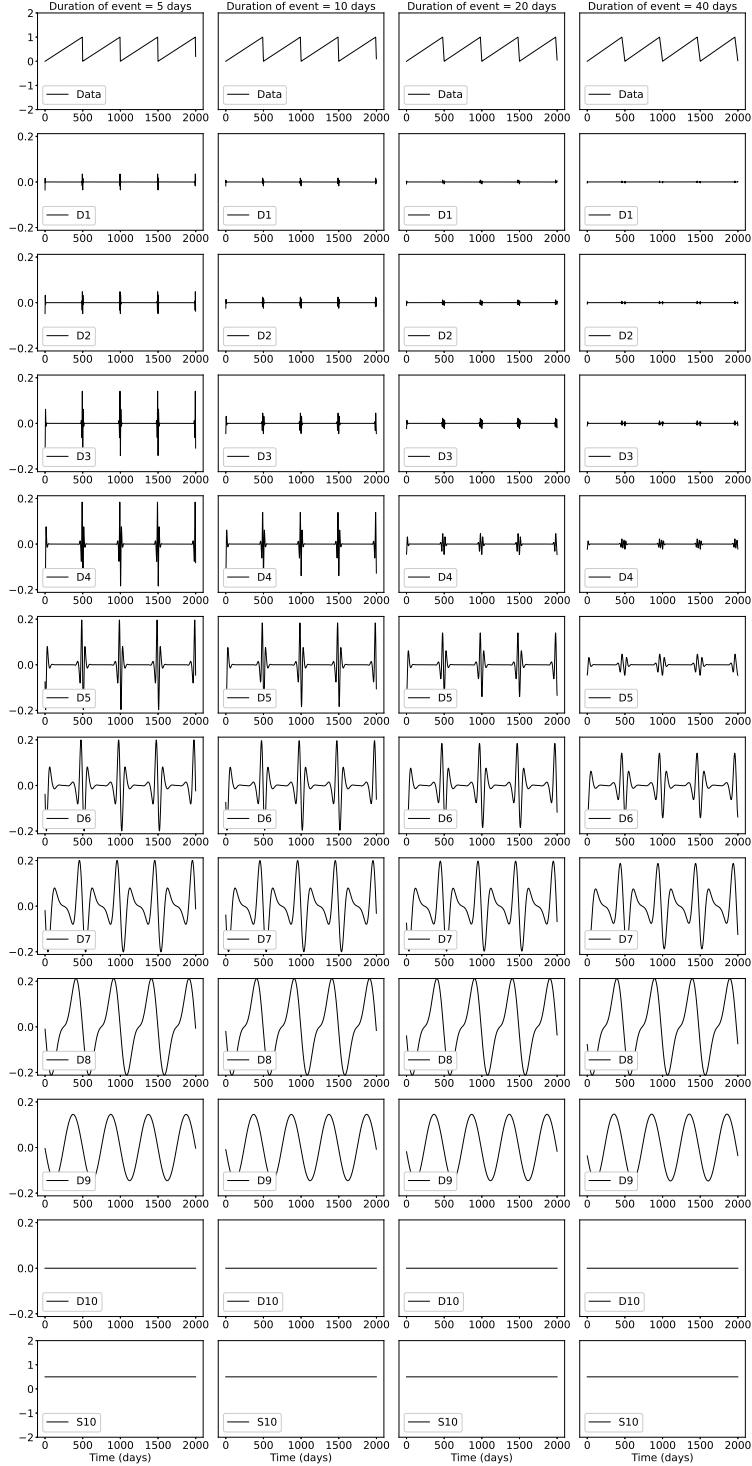


Figure 1: Demonstration of a wavelet decomposition for a synthetic dataset. A synthetic time series is created (top row) with steps of period 500 days, and transient durations of 2 days (left), 5 days, 10 days, and 20 days (right). The resulting details and smooths are shown in increasing level. The amplitude of the synthetic time series is normalized to 1, and the details and smooths show the relative amplitude.

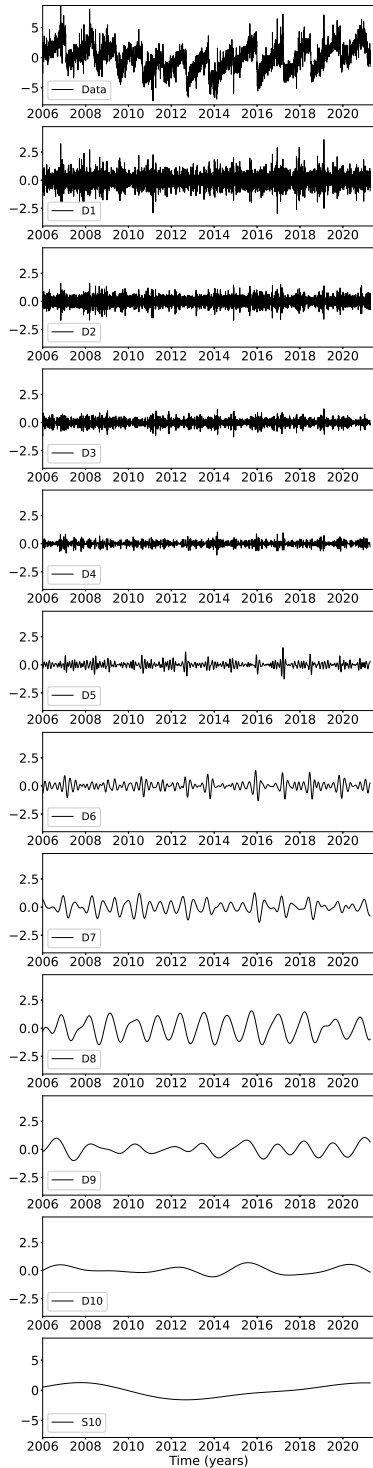


Figure 2: Top: Longitudinal displacement recorded at GPS station PGC5. The resulting details and smooth of the wavelet decomposition are shown in increasing level.

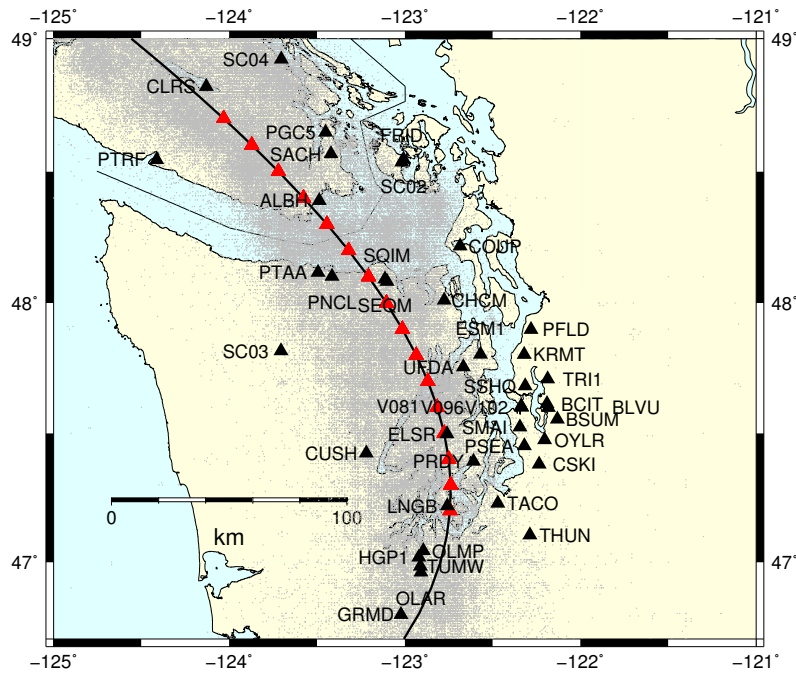


Figure 3: GPS stations used in this study (black triangles). The black line represents the 40 km depth contour of the plate boundary model by Preston et al. [2003]. The red triangles are the locations where we stack the GPS data. The small grey dots are all the tremor locations from the PNSN catalog.

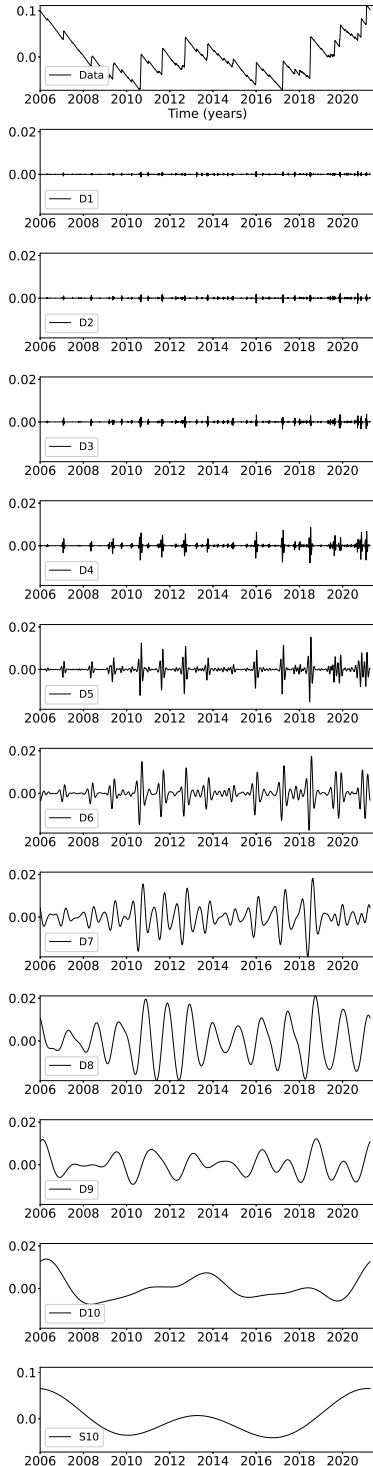


Figure 4: Details and smooth of the wavelet decomposition of the detrended cumulative tremor count around the third northernmost red triangles on Figure 3 (latitude 48.5).

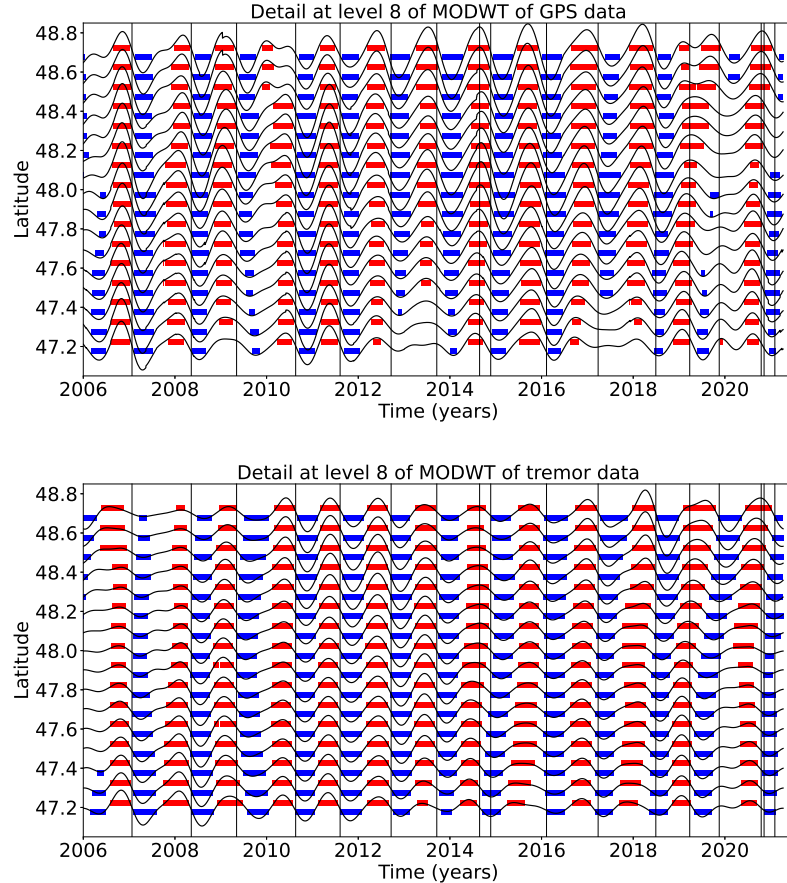


Figure 5: Top: Stacked 8th level details of the wavelet decomposition of the displacement over all the GPS stations located in a 50 km radius of a given point, for the 16 red triangles indicated in Figure 3. Bottom: 8th level detail multiplied by -1 of the cumulative tremor count in a 50 km radius of a given point for the same 16 locations. The black lines represent the timings of the ETS events from Table 1. We mark by a red rectangle every time where the amplitude is higher than a threshold of 0.4 (for the GPS) or 0.003 (for the tremor). We mark by a blue rectangle every time where the amplitude is lower than minus the threshold.

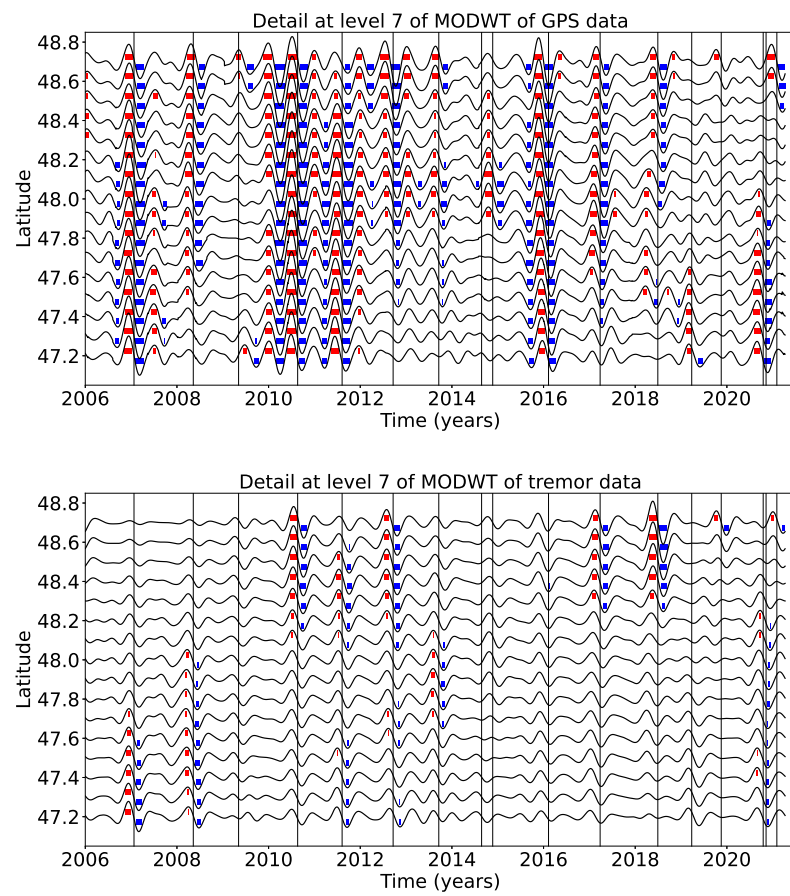


Figure 6: Same as Figure 5 but for the 7th level detail. The thresholds are 0.5 (for the GPS) and 0.01 (for the tremor).

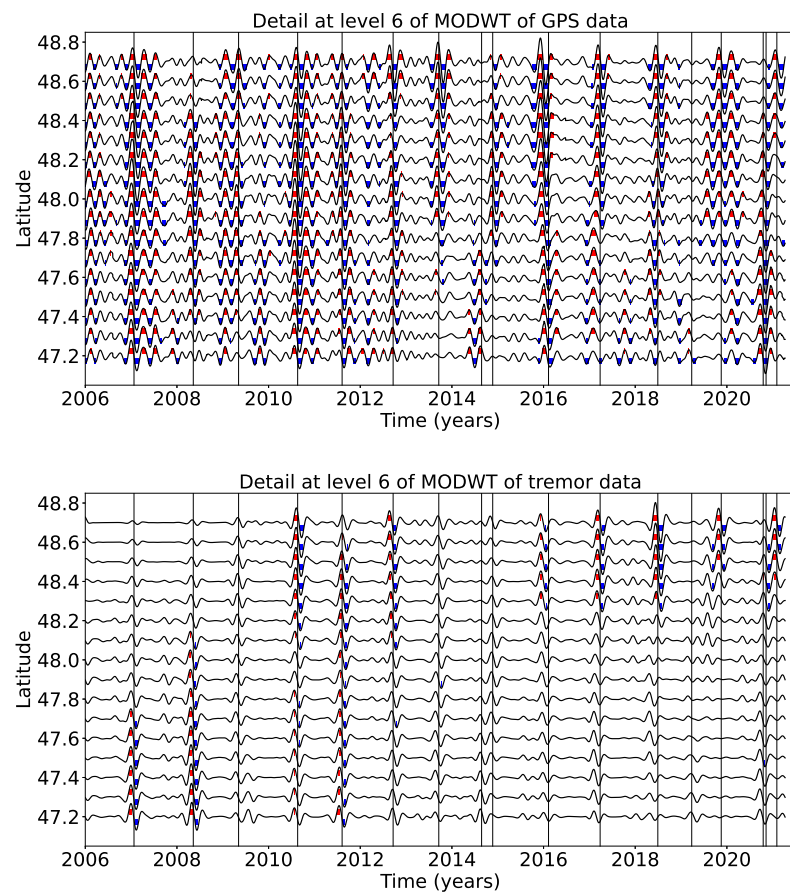


Figure 7: Same as Figure 5 but for the 6th level detail. The thresholds are 0.3 (for the GPS) and 0.009 (for the tremor).

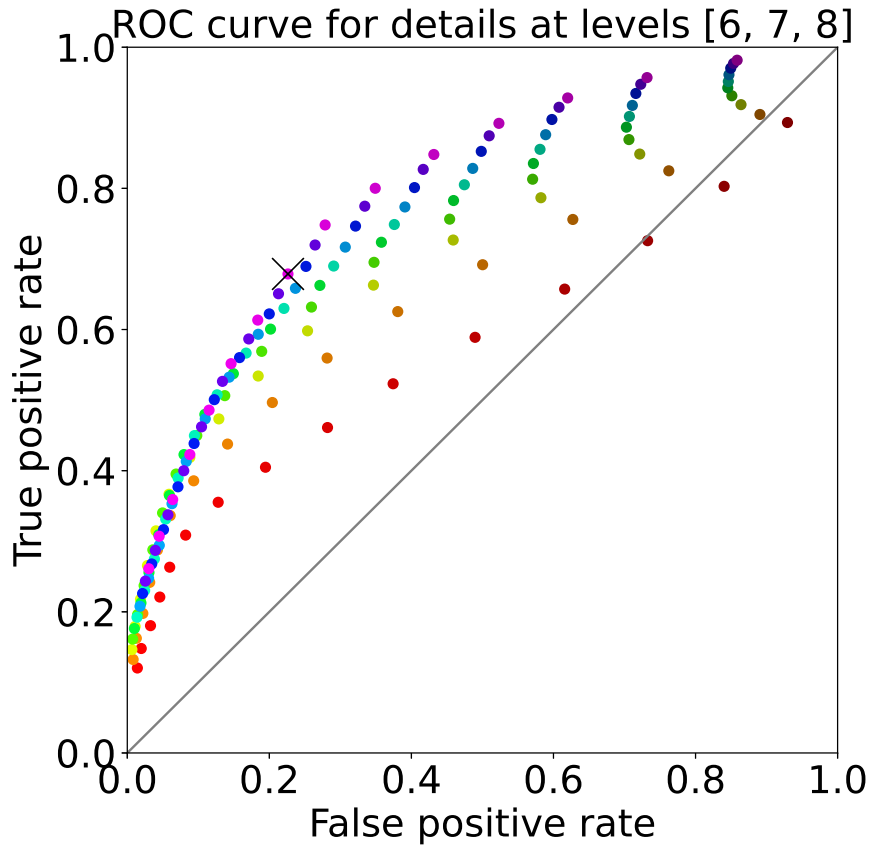


Figure 8: ROC curve for the sum of the 6th, 7th, and 8th level details of the wavelet decomposition. Each dot represents the true positive rate of event detections and the false positive rate of event detections for a given pair of thresholds (for the GPS and for the tremor). The **black cross** marks the true positive rate and the false positive rate obtained with the thresholds used to make Figure 9. **The values of the threshold are color-coded.** Reds correspond to the lowest value of the threshold for the tremor (0.001), while oranges, greens, blues, purples correspond to increasing values of the threshold for the tremor (up to 0.01). The brightest colors correspond to the highest values of the threshold for the GPS (1.5), while the darker and darker colors correspond to decreasing values of the threshold for the GPS (0.1).

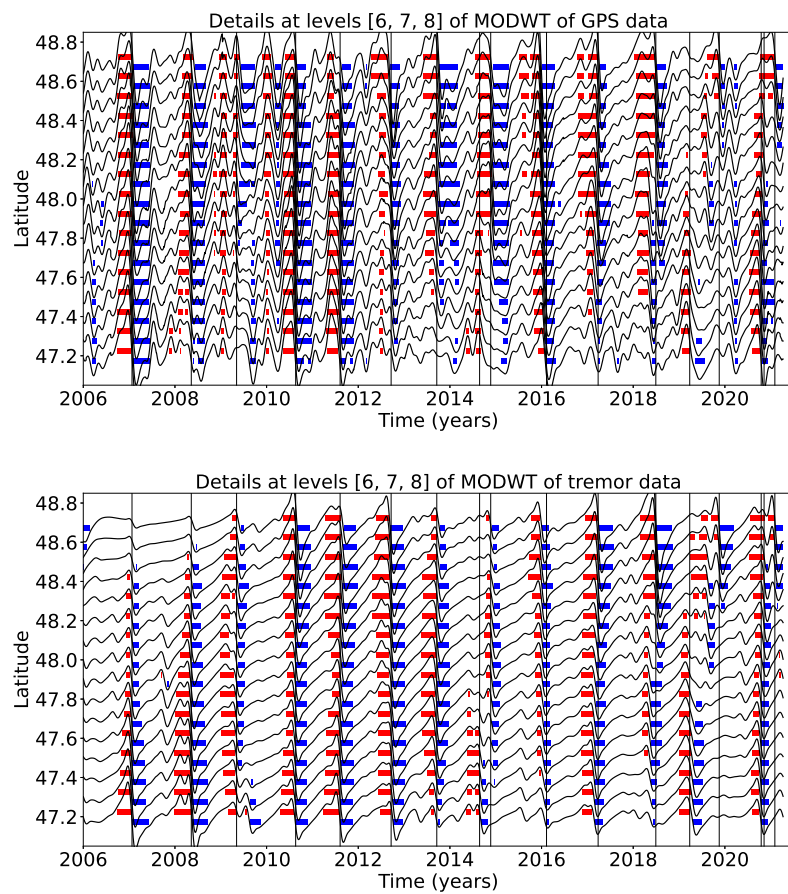


Figure 9: Same as Figure 5 but for the sum of the 6th, 7th and 8th level details. The thresholds are 0.8 (for the GPS) and 0.01 (for the tremor).

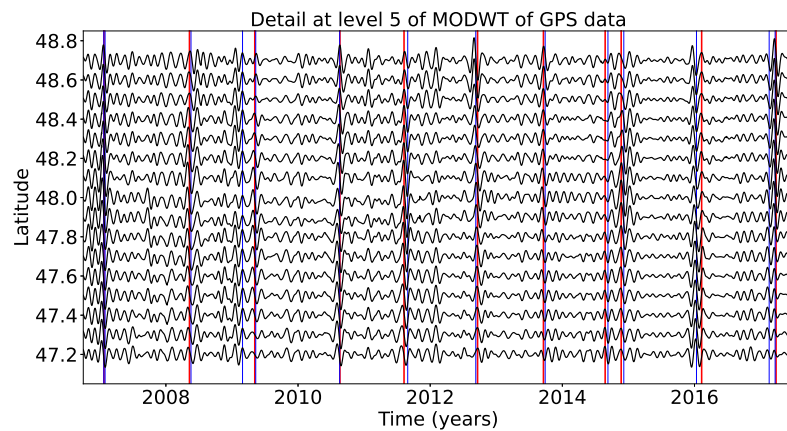


Figure 10: Top: Stacked 5th level details of the wavelet decomposition of the displacement over all the GPS stations located in a 50 km radius of a given point, for the 16 red triangles indicated in Figure 3. The red lines represent the timings of the ETS events from Table 1. The blue lines represent the timings of the magnitude 5 events from the catalog of Michel et al. [2019].

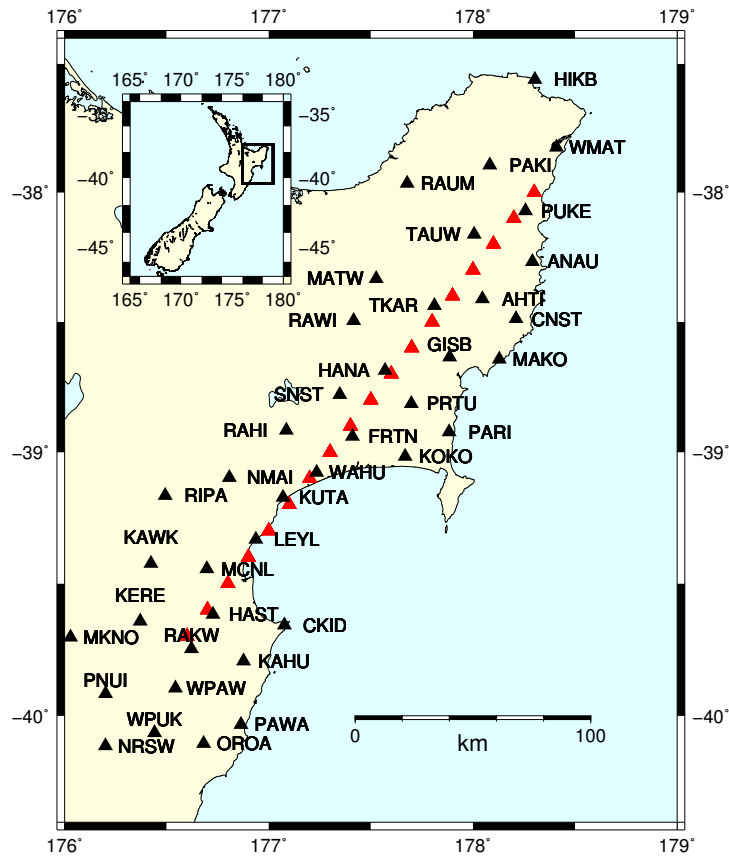


Figure 11: GPS stations used for the slow slip detection in New Zealand (black triangles). The red triangles are the locations where we stack the GPS data. They are located close to the 20 km depth contour of the plate boundary from Williams et al. [2013].

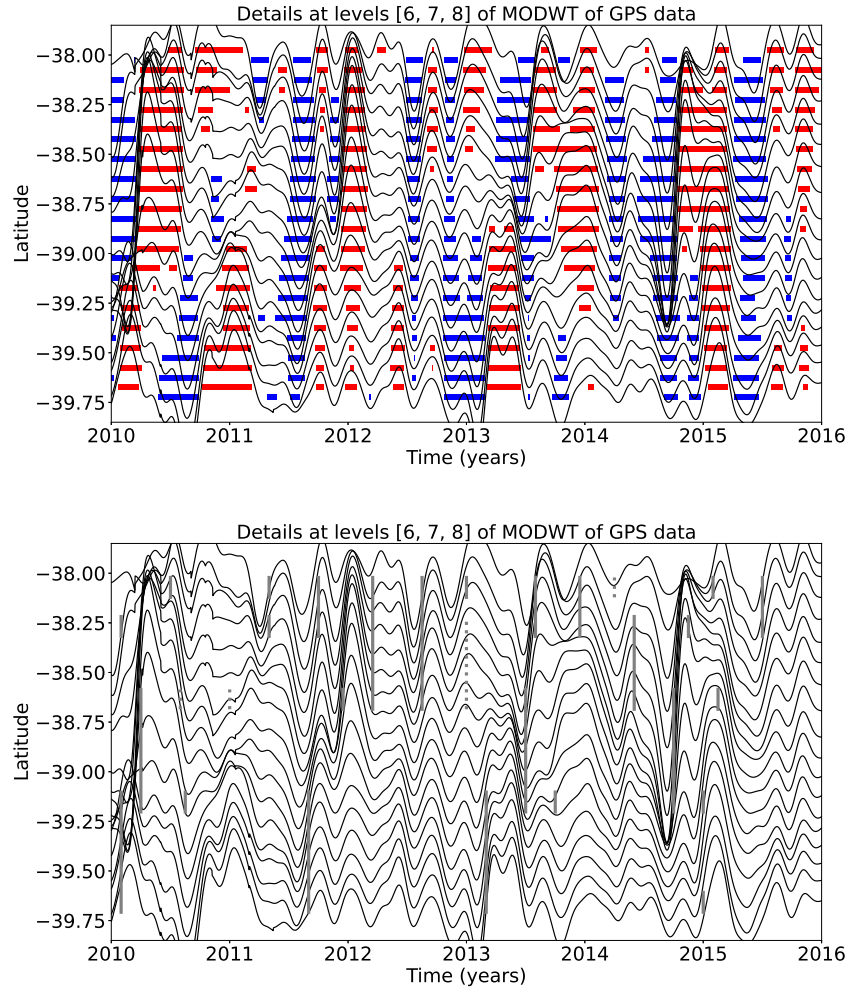


Figure 12: Top: Sum of the stacked 6th, 7th and 8th level details of the wavelet decomposition of the displacement over all the GPS stations located in a 50 km radius of a given point, for the 18 red triangles indicated in Figure 11. We mark by a red rectangle every time where the amplitude is higher than a threshold equal to 0.4. We mark by a blue rectangle every time where the amplitude is lower than minus the threshold. Bottom: Sum of the stacked 6th, 7th and 8th level details of the wavelet decomposition. We mark with a grey bar the slow slip events detected by Todd and Schwartz [2016].